Transient Polarization and Dendrite Initiation Dynamics in

Ceramic Electrolytes

Rajeev Gopal^a, Longan Wu^a, Youngju Lee^a, Jinzhao Guo^b, and Peng Bai^{a,c,*}

^a Department of Energy, Environmental and Chemical Engineering, Washington University in St. Louis, 1

Brookings Dr, St. Louis, MO 63130, USA.

^b Department of Mechanical Engineering and Materials Science, Washington University in St. Louis, 1

Brookings Dr, St. Louis, MO 63130, USA.

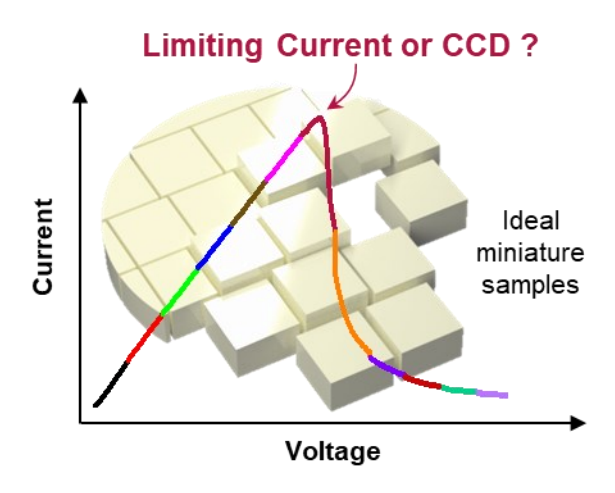
^c Institute of Materials Science and Engineering, Washington University in St. Louis, 1 Brookings Dr, St.

Louis, MO 63130, USA.

* Correspondence to: pbai@wustl.edu

Abstract

Solid-state-electrolytes combined with lithium metal anodes have the potential to improve the energy density of lithium-ion batteries. However, soft Li metal can still penetrate these stiff electrolytes above a critical current density (CCD). Prevailing methods to determine CCD suffer inconsistencies due to void formations after repeated stripping and plating, leaving significant variations in reported data. Here, we combine one-way linear sweep voltammetry (LSV) with electrochemical impedance spectroscopy (EIS) to uncover the existence of significant polarization in ceramic electrolytes, which can fully relax even without stacking pressure. At high scan rates, LSV experiments showed metal penetration with a diverging transient current, similar to CCD values. However, at a lowered scan rate, the transient current reaches a maximum, suggesting a dynamic electrochemical limiting mechanism. The results and analysis of many consistent samples suggest that polarization of mobile charge carriers preceding the maximum current is critical for accurately understanding dendrite penetration in ceramic electrolytes.



Lithium-ion batteries are the key enabling technology for portable electronics and electrical mobilities. Breakthroughs for increasing energy density are still critically needed. One promising route is the all-solid-state battery, in which a nonflammable solid-state electrolyte (SSE) is expected to stabilize the lithium (Li) metal anode and retard the chemical degradation of intercalation cathode to achieve higher energy density, better safety, and longer cycle life. However, metal penetrations through ceramic SSEs, most notably the garnet-type cubic Li₇La₃Zr₂O₁₂ (LLZO), have been reported in various operation conditions¹⁻³.

One of the most commonly used criteria to characterize the SSEs is the critical current density (CCD), which is determined in step-wise galvanostatic cycling of a Li|SSE|Li symmetric cell until a sudden voltage drop toward 0 V is observed^{4–6}. Multiple factors have been identified to influence the CCDs³, including porosity⁷, grain size⁸, grain dopants⁹, grain boundary modifications¹⁰, sintering conditions^{11,12} pellet defects^{13,14}, and electronic conductivity^{15,16}. Common to most studies, the repeated plating and stripping generate voids at the SSE|Li interfaces, therefore causing significant contact loss even under high stacking pressures^{13,17–19}. The differences between the true working current densities and the apparent current densities were difficult to quantify, leaving wide variations that impede rigorous theoretical analyses. In addition to the interfacial effects, the material and pellet properties of samples from different synthesis routes further complicated the identification of reliable correlations. Preparing ceramic materials and pellets in high consistency and large quantity and ensuring the accurate determination of true working current density are still outstanding critical challenges blocking the establishment of fundamental understandings of the CCD and the metal penetration dynamics.

Here, large quantities of highly consistent SSE samples were prepared and tested by oneway linear sweep voltammetry (LSV), combined with electrochemical impedance spectroscopy (EIS) measurements at different stages. We discover, for the first time, the existence, development, and recovery of transient concentration polarization in SSE pellets of various thicknesses that suggest a transport-limited mechanism preceding the dendrite initiation. It is worth noting that local heterogeneities have been reported in individual pellets²⁰. Despite using miniature samples from the same mother pellet, slight variances can still be observed. To ensure statistical significance, each test was conducted at least three times and the results are presented with error bars in both the main text and supplementary information.

The consistent critical current density. A major benefit of LSV is the absence of stripping, hence the formation of voids, at the working electrode, mitigating areal evolution commonly experienced by cycling experiments, where repeated stripping and plating promote void formation and localized current densities that can be several orders higher than the nominal apparent current density. Figure 1 shows our experimental setup and the typical results from LSV tests. To ensure high consistency of physical properties among SSE, ceramic pellets were fabricated using the same Li_{6.4}La₃Zr_{1.4}Ta_{0.6}O₁₂ (LLZTO) powder and sintered under the same conditions. Circular pellets were cut into parallel-faced pieces using a low-speed diamond saw (Fig. 1a). The miniature samples (approximately 2 mm × 2 mm × the desired thicknesses) were polished to remove any high-resistance carbonate or hydroxide surface layers and possible imperfections. Two opposite faces of the polished sample were coated with molten Li by a facile rubbing technique²¹ (Supporting Information Fig. S1). During electrochemical tests at 25 °C in an Argon-filled glovebox, a stacking pressure of 20 MPa was implemented to further ensure the intimate contact at the interfaces (Fig. 1b).

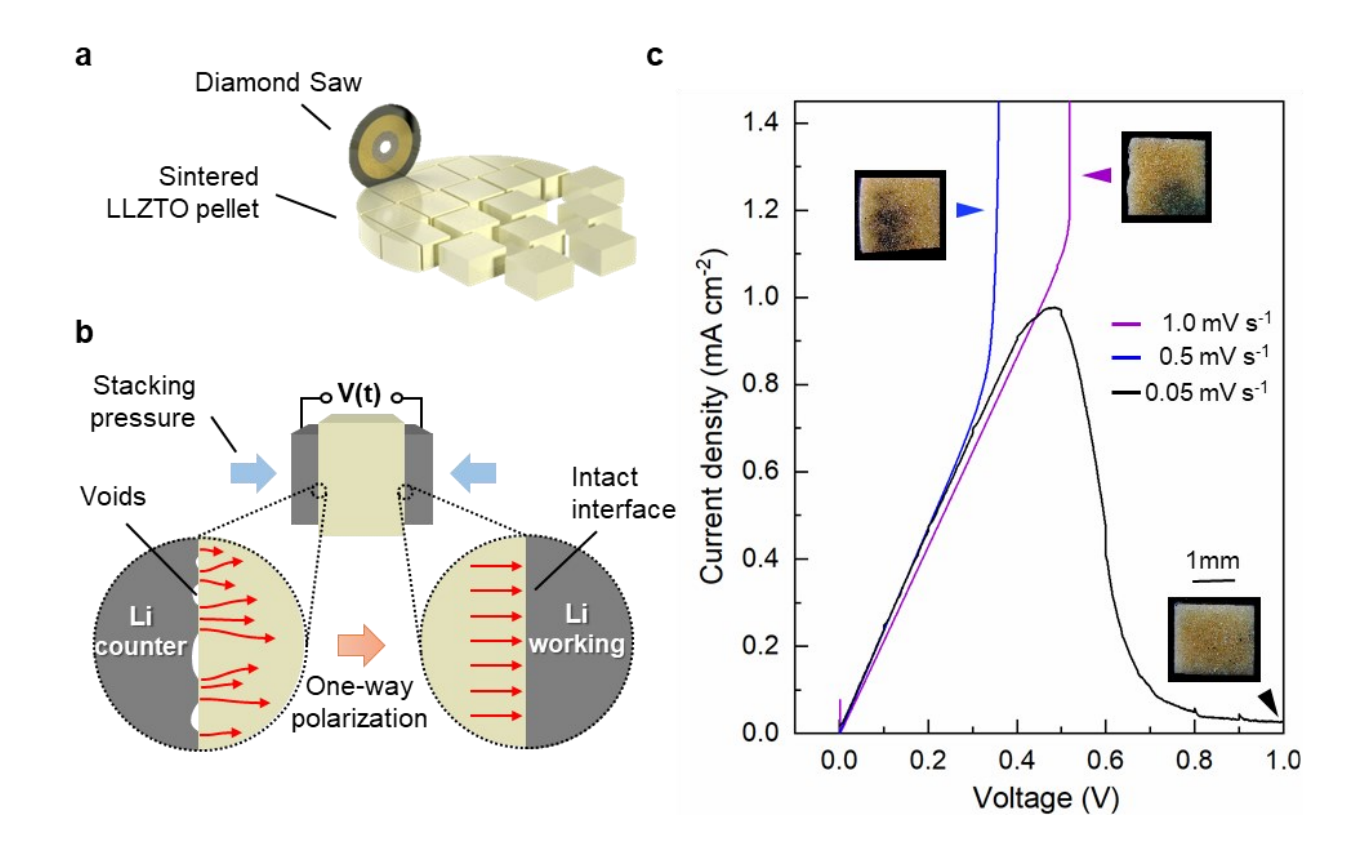


Figure 1. Linear sweep voltammetry experiments to determine the CCD in consistent miniature samples. Schematic of a, cutting multiple miniature samples from the same parent pellet (Supporting Information S2b), b, and testing a Li|SSE|Li symmetrical cell under the one-way polarization. Red arrows represent the Li-ion flux streamlines. A stack pressure of 20 MPa was maintained during the test, preventing delamination of the working electrode. c, Linear sweep voltammograms were obtained from samples with a relative density $\geq 95\%$ at scan rates of 1, 0.5, and 0.05 mV s⁻¹. The inset digital photos show the surface of the SSE sample at the working electrode, where black regions are the residual metal penetration structures through the sample. No penetration structure was observed in samples that developed the limiting current peak, at the scan rate of 0.05 mV s⁻¹.

As the voltage increases, the transient current exhibits a linear Ohmic response, yielding a total conductivity consistent with impedance measurements (0.6 mS cm⁻¹, Supporting Information Fig. S1). For samples tested at scan rates of 1 mV s⁻¹ and 0.5 mV s⁻¹, the transient current diverges around 1 mA cm⁻², manifesting metal penetration at the CCD (Fig. 1c and the inset photos with dark regions). As a result of much less contact loss at the working electrode (Supporting Information

Fig. S2), the CCDs determined here by LSV are higher than those reported in the literature studying the same material with the same configuration using the galvanostatic cycling method. Surprisingly, however, when the scan rate was lowered to 0.05 mV s⁻¹, the increase of transient current was self-limited around 1 mA cm⁻² to form a peak, followed by a smooth decay toward a stable value, resembling the typical LSV responses of liquid electrolytes^{22,23}.

To ensure fair comparisons with the literature data obtained from two-electrode systems ^{4,13,15,18,24–29} we use the two-electrode configuration in our LSV tests. The relatively easier fabrication procedures of the two-electrode cells also allow us to obtain reliable experimental results in large quantity. However, similar phenomena that the transient current reaches a maximum at low LSV scan rates were still observed in our three-electrode setup (Supporting Information Fig. S3), which has not been rigorously used by previous studies in testing LLZO.

Impedance evolution near the current peak. In stark contrast to the diverging current at higher scan rates due to penetration (inset photos in Fig. 1c), the current peaks observed at low scan rates suggest a limiting mechanism, which may be attributed to the decrease of conductivity (due to concentration polarization) and the loss of interfacial contact (due to void formation at the counter electrode). To decipher the dynamics behind the transient current, we repeat the LSV test but paused it intermittently every 50 mV and held at that voltage value to complete a concurrent EIS test. Here, a frequency range of 600 kHz to 10 Hz was adopted to ensure a short testing time of about 90 seconds, such that the state of the ceramic electrolyte will not change significantly during the voltage hold. The obtained LSV curve showed negligible deviations at these checkpoints, while the limiting current peak still emerged (Fig. 2a). Typical Nyquist plots are shown in Supporting Information S4a and S4b. A separate experiment was performed without any EIS pauses to assess any possible effects on the subsequent voltammogram. As shown in

Supporting Information S5, no substantial differences were observed. The choice of frequency range is sufficient to detect the targeted bulk behavior. Interestingly, the EIS spectra collected in the Ohmic region (before 250 mV) are nearly identical (Fig. 2b). Right after the current peak, however, a significant increase in impedance was discovered. Quantitative analyses by fitting the spectra to a widely used equivalent circuit model revealed the increase of impedance or decrease of conductivity, mainly occurred at the interface and the low-frequency contribution region (Supporting Figure S4d). Note that the small depressed semi-circle obtained at the very low frequencies has been shown in many studies but has yet to be linked to clear physical processes ^{18,30}. The capacitance values were found by fitting the distorted semi-circle by the constant phase element (CPE), calculated by Eq. S1 in Supporting Information. The bulk and grain boundary impedances appear as one convoluted contribution ³¹, attributable to the high quality (relative density and conductivity) of our pellets, with the resistance remaining relatively constant throughout the experiment.

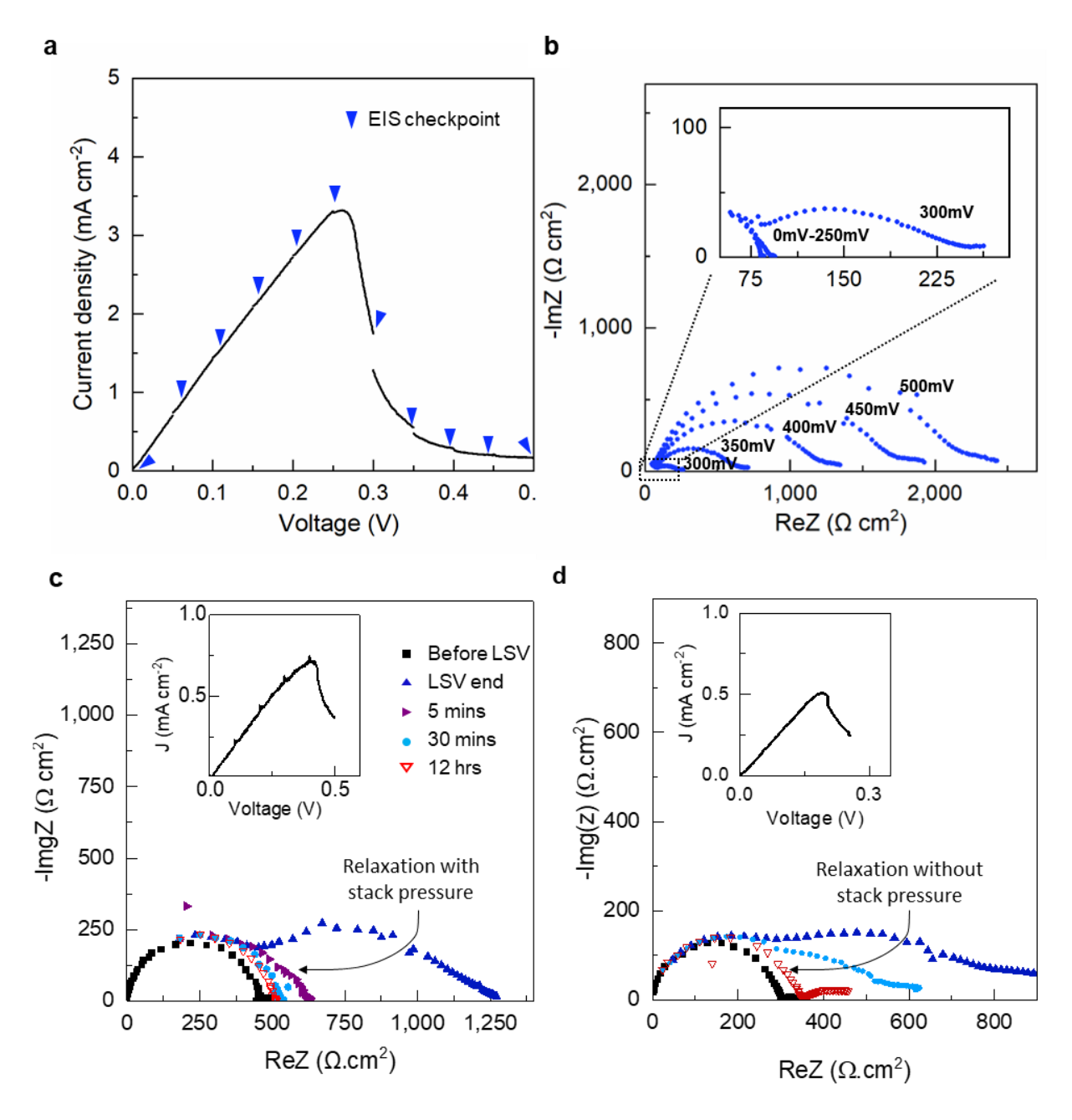


Figure 2. Results of the combined LSV and EIS measurements of the symmetric cells. a, Voltammogram showing the limiting current peak with blue arrowheads indicating the checkpoints for quick EIS measurements. b, Corresponding EIS spectra obtained at each checkpoint shown in panel (a). The total resistance shown by LSV is consistent with the EIS value (Supporting Information Table S1). Details of the fitting are available in Supporting Information Fig. S4. Relaxation behaviors revealed in separate LSV-EIS experiments c, with stack pressure (extracted data in Supporting Information Table S2) and d, without stack pressure that were stopped after the limiting peak current (additional data in Supporting Information S6). Insets show the corresponding voltammograms.

In liquid electrolytes, the transition from the Ohmic region to a current peak, then a stabilized current, is caused by transport limitation²³. For SSEs, however, the common belief is that the fixed background charge from the static crystal structure ensures a near-unity transference number, such that long-range concentration polarization and therefore the transport limitation should not occur. During concentration polarization, fewer and fewer mobile lithium ions are available at the working electrode interface to maintain the original conductivity, leading to a lower subsequent total current and hence a higher measurable resistance, and eventually a transport limitation as reflected by the decreasing transient current.

To investigate whether the impedance increase is a transient behavior that can be attributed to transport, a separate LSV experiment was performed and stopped right after the current peak to monitor the impedance evolution during relaxation. These relaxation tests were performed with and without pressure to determine whether the stacking pressure may influence the interface and the subsequent relaxed impedance. The pressure removal took less than 10 seconds and was done immediately at the end of the LSV (additional results in Supporting Information S5). As shown in Fig. 2c and 2d, the impedance indeed recovered to the original value. Most surprisingly, the relaxation process without stacking pressure proceeded the same way. Had there been any voids formed at the SSE|Li interfaces, the 20 MPa we applied may not be adequate to cause the creep of Li metal to fill the voids, not to mention a recovery process without stacking pressure. The results not only rule out the possibility of void formations as the reason of the LSV current peak, but also suggest that the significant impedance increase was a reversible polarization and can diminish upon the removal of the electrochemical driving force. Following the basic principle of conductivity, where the concentration and mobility of the free charge carriers are the two dominant factors³², the transient but significant changes in the impedance suggest that it was the polarization of mobile Li ions at the interface that induced the lowered conductivity. Once this polarization driving force is removed, Li ions would return to their equilibrium concentration and the original conductivity is restored. As we shall discuss in detail in the section of *Concentration polarization preceding dendrite initiation*, the similarity of concentration polarization between the ceramic electrolytes and the liquid electrolytes are tell-tale signs of a unifiable transport mechanism leading to the Li dendrite penetration.

Characterization of interfaces. Li growths into, or protrusions out of, SSEs can cause localized ionic flux that may lead to increased impedance and inaccurate calculation of the current densities. Before a rigorous transport analysis can be performed, interfacial contact quality between Li metal and the SSE, especially at the interface of Li plating, must be verified experimentally. Using scanning electron microscopy (SEM), cross-sectional images (Fig. 3c-f) at the working and counter electrodes from four samples, i.e. before the LSV and stopped at three different points of the LSV (Fig. 3a), were obtained. The images at 0 V (Fig. 3c) and 0.4 V (Fig. 3d) show intact interfaces fully wetted by Li metal. However, the sample stopped at 0.8 V developed clear voids at the counter electrode (Fig. 3f). For line cuts of the large two-dimensional (2D) interface. Therefore, impedance characterizations of the entire electrode, as an electrochemical response directly relevant to the operation conditions, are more reliable. The impedance spectra of the entire mm-scale electrodes are consistent with the SEM results. For the samples obtained at 0 V, 0.4 V, and 0.6 V, the significantly increased impedance can recover to the original values when the cells are fully relaxed (Fig. 3b), but the sample stopped at 0.8 V only partially recovered, leaving a wide depressed semi-circle that is consistent with the irreversible changes observed in SEM (Figs. 3b and 3f).

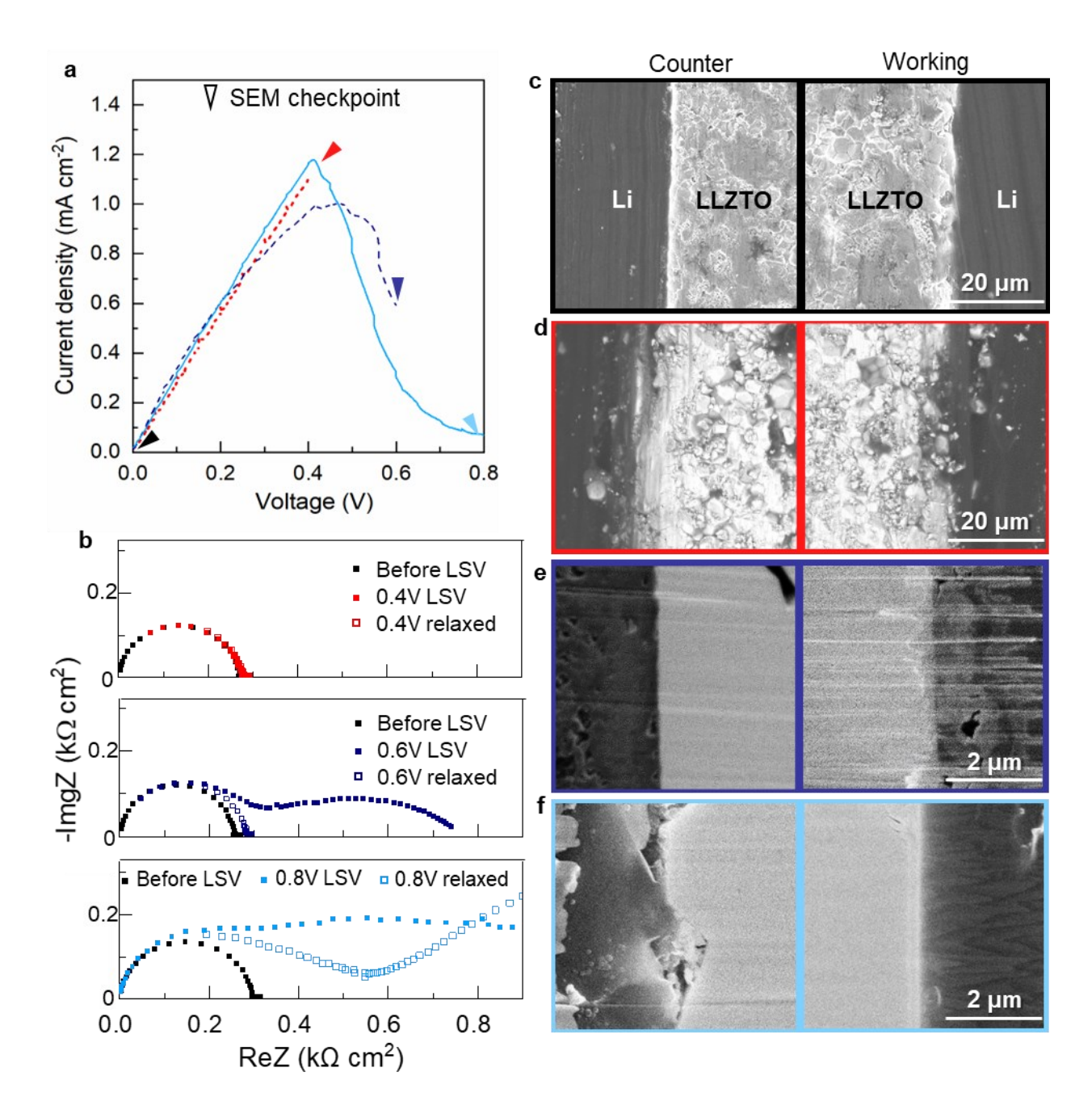


Figure 3. Impedance and postmortem scanning electron microscopy (SEM) characterizations of the interfaces at different stages of the LSV. a, Voltammograms of samples tested in separate LSV experiments that were stopped at different stages indicated by the color-coded arrowheads. b, Transient and relaxed impedance spectra of the three samples. For the 0.6 V sample, the increased transient impedance (dark blue) can recover close to the original equilibrium state while the 0.8V (light blue) sample shows much higher transient increases which cannot fully recover. Fitting results in Supporting Information Table S3. c-f, Side-view SEM images of the interfaces at the counter and the working electrodes of samples obtained at (c) 0 V, (d) 0.4 V, (e) 0.6 V, and (f) 0.8 V. The interfaces of the critical case of 0.6 V and 0.8

V were prepared by focused ion beam (FIB). Other samples were prepared by fracturing the Li|SSE|Li cell with a sharp blade.

Effects of bulk microstructure. To ensure the generality and reliability of our discovery, we performed the same experiments with samples of varied relative densities. While we propose here that the transport limitation reached at the interface will initiate dendritic growth, this mechanism will only be uncovered if other factors do not over-shadow this mechanism. One such factor is the porosity which is tied to the relative density of the sintered pellet. A low relative density and the higher propensity of interconnected pores have been shown to promote dendrite formation and ultimately lower CCDs⁴. While the relative density appears as merely an averaged geometric property, it provides an effective single metric that quantifies the overall quality of the pellet, yet physically reflects multiple aspects of the microstructure that influence the metal penetration behavior at the CCD.

As displayed in Supporting Information Fig. S7a-c, an increase in the relative density led to the reduction in sizes and numbers of pits on the polished top surfaces. Samples at 99% relative density (99 rd%, versus the theoretical density of 5.491 g cm³) and at 91 rd% show contrasting top-view surface features, while samples at 95 rd% appear similar to those at 99 rd%. Fractured cross-sections reveal higher internal packing density and better grain connectivity as the relative density increases. Samples at 95 rd% and 99 rd% exhibit sharp edges of intra-particle fracture, indicating well-formed grain boundaries. Higher relative densities enable higher total ionic conductivities, as reflected by the slope of the Ohmic region (Supporting Information Fig. S7d).

Although a relative density of 91% only indicates a slight porosity, penetrations with diverging current spikes always occur, yet at relatively low current densities. Samples at 99 rd%

did not encounter any current spikes, regardless of thickness, unless stronger dynamic excitations (e.g. higher scan rates) are implemented. For samples at 95 rd%, about 10% encountered penetrative current spikes, while the rest developed the limiting current peaks. However, the CCD values determined at the onsets of the current spikes (seen in LSV with higher scan rates) are very close to those of the current peaks (seen in LSV at a scan rate of 0.05 mV s⁻¹). The metal penetration through samples with lower relative densities may be attributed to the excess free electrons on pore walls that can reduce mobile lithium ions under the localized electric field and thereafter promote dendritic metal penetration^{15,16}. Lower relative densities may lead to percolated pores for metal filaments to grow through⁴.

While the 0.5 mm-thick samples would yield an Ohmic slope steeper than the 1 mm-thick samples, as dictated by their respective total conductance, it is difficult to explain why thinner samples would also enable a much higher peak current if the key physics of the CCD is governed solely by an interfacial process. The inverse relationship between the electrolyte thickness and the peak current is true for both the 95 rd% and 99 rd% samples. Even at 91 rd%, 0.5 mm-thick samples have higher CCDs than the 1 mm-thick ones. Therefore, the total conductance, i.e. the long-range transport process, appears to play a critical role in the CCD.

Peak currents at different scan rates. According to the Randles-Sevcik equation (Supporting Information Eq. S2) that explains the transient current from LSV tests of liquid electrolytes⁴⁷, the peak current is scan-rate-dependent, and the scaling between the peak current (I_p) and the scan rate (v) should yield a power-law exponent of 0.5, i.e. $I_p \propto \sqrt{v}$. Here, we chose 1-mm-thick miniature pellets to repeat the LSV experiments, but at much lower scan rates. As shown in Supporting Information Fig. S8, peak currents were still observed. The fitting of these peak current densities (J_p) against the scan rate (v) follows a power-law scaling well (Fig. 4a).

Replotting the data to enforce the power-law fitting of the Randles-Sevcik equation yields a goodness of fit of R²=0.964 (Fig. 4b). Despite differences between the SSE and liquid electrolytes, the fitting results suggest that the limiting mechanisms at the current peaks are close to the transport-limited mechanisms in the liquid electrolytes, based on which the Randles-Sevcik equation was developed.

Theoretically, the transient currents in response to different scan rates should eventually converge to the same limiting current at higher voltages. However, due to the interfacial damage soon after the peak (as revealed in Fig. 3f), the decaying current after the peak from each experiment is difficult to be converted to an accurate current density for cross-system comparison. As an alternative, a small enough scan rate may induce a peak current that is sufficiently close to the true limiting current. Here, we chose a scan rate of 0.003 mV s⁻¹ to examine the transient current and defined the obtained peak current density as the quasi-limiting current density to approximate the true limiting current density.

Concentration polarization preceding dendrite initiation. The limiting current density is system-specific. As demonstrated in liquid electrolytes ^{33–35}, only when an over-limiting current density (i.e. higher than the limiting current density) is applied to the liquid systems, and the Sand's time is reached upon the complete depletion of ions at the electrode surface, would the tip-growing, fast-advancing, fractal dendrite start to form³³. Testing the thickness-dependence of the system-specific limiting current density is another compelling approach to verify the hypothesis of the limiting mechanisms of the peak currents. Here, pellets with relative densities higher than 95% were cut and polished to reach different thicknesses of around 0.5 mm, 1 mm, 2 mm, and 3 mm. LSV experiments at scan rates of 0.05 mV s⁻¹ and 0.003 mV s⁻¹ were then performed until either a current spike indicating penetration or a current peak indicating transient limitation was observed.

The scan rate of 0.05 mV s⁻¹ is the highest scan rate to induce the current peaks that are comparable with the CCD values, while 0.003 mV s⁻¹ is the lowest feasible scan rate that we chose to induce the quasi-limiting current density to probe the system properties. These two types of characteristic current density values were then plotted against the thicknesses of the samples (Fig. 4c and 4d). Corresponding voltammograms can be found in Supporting Information Fig. S9 and S10. Note that chronopotentiometry experiments with values higher than the peak current density obtained at 0.05 mV s⁻¹ always led to metal penetrations (Supporting Information Fig. S11), which further proves that the peak current reflects the same physical property as the traditional CCD does. Both the peak current density obtained at 0.05 mV s⁻¹ and the CCD of the traditional definition (with observed penetration) are referred to as the generic CCD.

As shown in Figs. 4c and 4d, the two types of characteristic current densities, i.e. CCD and the quasi-limiting current density, are inversely proportional to the thickness of the SSE pellets. This trend coincides with that of liquid systems, where the system-specific limiting current density³³ is strictly proportional to the reciprocal of the electrolyte thickness via $J_{lim} = 2zFDC_0[(1-t_+)L]^{-1}$. Here, z is the charge number, F the Faraday constant, D the ambipolar diffusion coefficient, C_0 the bulk ion concentration, t_+ the lithium-ion transference number, and L the thickness of electrolyte.

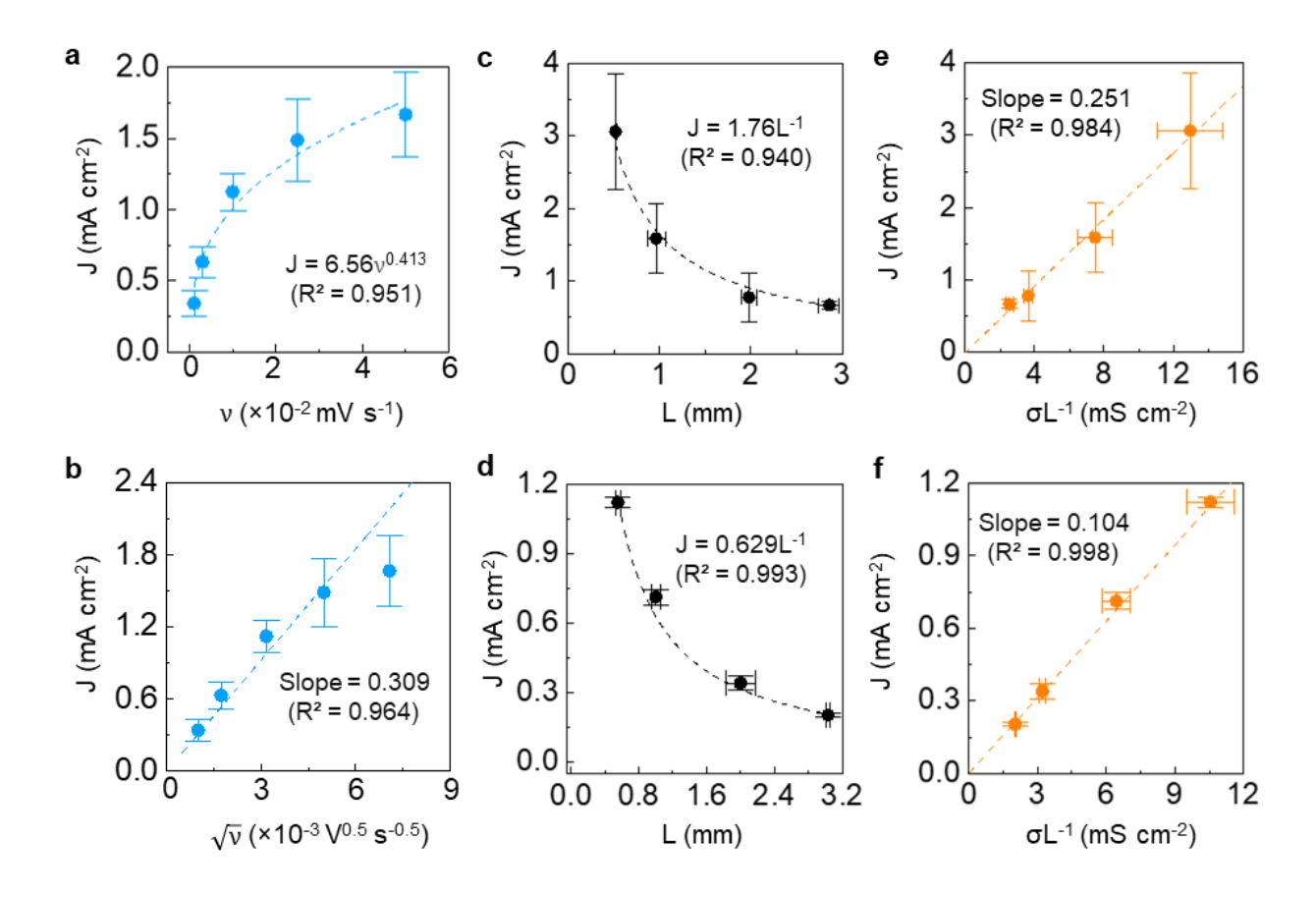


Figure 4. Scan-rate dependence of the peak currents determined by LSV and thickness-dependence of the diffusion-limited current densities. a, Plot of peak current densities versus scan rate for 1 mm samples shows an emergent power-law relationship, b, Randles-Sevcik plot to reveal the linear correlation between the peak current and the square root of the scan rate, indicating diffusion limitation. c, Plot of CCDs against pellet thicknesses. d, Plot of quasi-limiting current densities against pellet thicknesses with the mean values determined by grouping similar thicknesses. Plots of (e) CCDs and (f) quasi-limiting current densities versus the thickness-adjusted conductivities, according to Eq. (1). Error bars show standard deviation of the data.

To understand the physics behind this correlation that resembles the correlation in liquid electrolytes, we implemented the Nernst-Einstein relation to convert the total conductivity to an effective "total" diffusion coefficient, $D^{\sigma} = \sigma RT C_0^{-1} z^{-2} F^{-2}$. Here, T is the temperature, R the

gas constant, and σ is the total ionic conductivity of the LLZTO sample. Substituting D^{σ} into the formula of limiting current density for dilute binary electrolyte yields a new equation:

$$J_{lim}^{\sigma} = \frac{2RT\sigma}{z(1-t_{+})FL} \tag{1}$$

This new limiting current density based on ionic conductivity suggests a data analysis method by plotting the characteristic current densities versus σL^{-1} . As can be seen in both Fig. 4e and Fig. 4f, each thickness-dependent data set collapses onto a single linear fitting line. It must be pointed out that, while the peak current obtained at a scan rate of 0.05 mV s⁻¹ also came from the same limiting mechanism, it is the one obtained at the sufficiently low scan rate that can approximate the true limiting current density of the SSE. Therefore, only the fitting slope in Fig. 4f was used to estimate the transference number of lithium ions in our LLZTO pellets, as discussed below.

Transference number and the mobile charge carriers. The transference number of lithium ions in ceramic electrolytes is expected to be a value very close to 1, as lithium ions are believed to be the only significant mobile charge carrier in ceramic electrolytes. While there indeed exist works investigating the Li vacancies³⁶ (effective negative charge carriers) in ceramic electrolytes that greatly facilitate the transport of Li ions, they were not taken into account in the discussion of the transference number. The widely used definition of t_+ for ceramic electrolytes considers instead the leakage electrons as the only negative charge carrier. Therefore, t_+ is calculated as the ionic current divided by the sum of the ionic current and the electronic current. When the leakage electronic current is negligibly small, the definition leads to a near-unity t_+ . The concentration and mobility of the Li vacancies may be low and hard to be determined³⁶, but their existence is critical for fast Li-ion conduction. Even if electrons must be considered in the case of ceramic electrolytes^{15,16}, they should not be the only negative charge carrier, excluding the contribution

from the effectively negative Li vacancies³⁶. The good agreement between the experimental data and Eq (1) that originated from liquid electrolytes suggests the binary-electrolyte characteristics in ceramic electrolytes.

The rigorous and proven definition of Li-ion transference number for binary liquid or polymer electrolytes^{33,37–39} reminds us that t_+ is bounded with the ambipolar/total diffusion coefficient 40 via $D/(1 - t_+) = 2D_+$. Wherever the self/tracer diffusion coefficient of Li ions (D_+) can be determined, it is not necessary to use this secondary quantity of t_+ for the transport analysis. As exemplified in our Supporting Information Table S4 and Eq. S2-S5, using the tracer diffusion coefficients reported in the literature, we were able to determine the concentration of mobile Liions in LLZTO to be around 20 M, by using the Randles-Sevcik slope presented in Fig. 4b, which is consistent with recent estimations 14,32. With the concentration and the tracer diffusion coefficient, the "true" limiting current density for our LLZTO pellet is determined to be around 0.27 mA cm⁻², which is consistent with our expectation that our quasi-limiting current density obtained at the lowest feasible scan rate is slightly higher than the true limiting current density. Note that we have applied in Eq (1) a simple assumption of $DH_R^{-1} = D^{\sigma}$, following the suggestion⁴¹ that the Haven ratio (H_R) between the tracer diffusion coefficient (D_+) and the one derived from the ionic conductivity (D^{σ}) is a constant smaller but close to 1. However, for Li-ion conducting ceramic electrolytes, the Haven ratio may vary in the range $^{42-44}$ of 0.24-0.7, resulting in a transference number in the range of 0.881 - 0.654, which are still more than two times higher than those determined from the liquid electrolytes.

The thickness dependence revealed by Eq (1) suggests that thinner SSEs have higher intrinsic limiting current densities (J_{lim}^{σ}). As demonstrated by Hitz et al.⁴⁵, when the net flux of Li-ions (collected from the porous layer of their trilayer LLZO electrolyte) travels through a dense 15 μ m

layer, their cells can continuously cycle at a high current density of 10 mA cm⁻². Assuming the same correlation presented in Fig. 4d, a thickness of 15 μ m yields a quasi-limiting current density of order 40 mA cm⁻². Therefore, a current density of 25% J_{lim}^{σ} will not trigger diffusion limitation and thereafter the dendrite penetration, as long as the intimate contact at the interfaces can always be maintained. As typical separators wetted by liquid electrolytes are designed to be around 20 μ m thick to avoid diffusion limitation, thinner SSEs, besides the benefits of lower total resistance and less inactive mass, will help avoid the significant concentration polarization and dendrite initiation at diffusion limitation.

Upon ion polarization, a space charge layer (SCL) can form in liquid electrolytes. Similar behavior of ion polarization and SCL at the SSE|Li interface have also been predicted through thermodynamic analysis⁴⁶. However, under dynamic electrochemical conditions, the thickness of SCL at the SSE|Li interface can extend into the SSE for hundreds of nanometers⁴⁷, as revealed by operando electron holography⁴⁸. Regardless of the specific thickness, the voltage change across a length scale in the range of 1nm to 1µm would generate a significant electric field, e.g. 1.3V across 10 nm from ref⁴⁹ yields 130 MV m⁻¹, which can easily break down most insulating materials⁵⁰. In liquid electrolytes, the significantly lowered salt concentration at diffusion limitation leads to decreased electrical conductivity and amplified local electric field⁵¹, which drives fast electrokinetic flows⁵² and electrode instabilities⁵³. In solid electrolytes, the SCLs at the macroscopic SSE|Li interface are connected with the grain boundaries where rich defects usually facilitate fast ion transport, therefore, forming a facile ion conduction path, where apparent limiting current can occur³⁸ even with a unity transference number. The enormous local electric field at the diffusion limitation will lead to easy electron injection⁵⁰ through the vulnerable ion conduction path to reduce the mobile Li-ions, either at the electrode surface or at the grain boundaries in the

bulk^{15,16}. The critical process may also be understood effectively as the result of an induced mechanical pressure at the interface³⁸ that can create cracks through the electrically insulating ceramic single crystals^{54,55}. While the observable dendrites or filaments grown after the diffusion limitation (induced by either high currents or large voltage bias) are indeed fundamentally different in different electrolytes^{15,56}, their appearances do not reject the rationale that the concentration polarization processes preceding the diffusion limitation are essentially the same for ceramic, polymer, and liquid electrolytes.

Void formations and the depletion of the intimate contact layer at the counter electrode can lead to the decrease of transient current, which may be misinterpreted as a transport limitation. In addition to the relaxation experiments without stacking pressure presented above, analyzing the capacity accumulated till the peak current can also rule out the possibility of void formation. Given the same Li|LLZTO interface preparation method, the same stacking pressure, and the similar thicknesses of the resulting Li metal layers, the intimate contact layer of Li metal at the counter electrode should be of similar thickness. Depletion of these similar contact layers should result in a similar characteristic capacity. However, as shown in Supporting Figure S12, we did not observe such a common capacity at the current peaks of our LSV experiments. On the contrary, the capacity at the current peaks shows a clear dependence on the thickness of the pellets, which suggested effects from the long-range transport.

By combining one-way linear sweep voltammetry with impedance diagnosis, we have demonstrated a new method of determining the CCD that can (i) avoid the contact loss encountered in the conventional galvanostatic method, and (ii) decouple the transient behaviors to contributions from the bulk, through the grain boundary, and at the interfaces of the ceramic electrolyte. Our electroanalytical tests of miniature samples with high consistency revealed, for the first time, the

existence of limiting current peaks that did not induce metal penetrations yet manifest a scan-ratedependent transport-limited behavior that can be fitted by the Randles-Sevcik equation for analyzing liquid electrolytes. The transient impedance spectra confirmed the development and the subsequent reversible recovery of significant concentration polarization at the macroscopic Lielectrolyte interface, but not in the bulk, of the SSE pellets. Despite the distinct differences between ceramic electrolytes and liquid electrolytes, our results suggest that the limiting mechanism that leads to the peak current in ceramic electrolytes can be understood by the classic theory for binary liquid electrolytes. While thinner SSEs are preferred for the reasons of lower total resistance and higher gravimetric and volumetric energy densities, our results offer the most critical consideration as thinner SSE is vital to ensure a higher intrinsic limiting current density and CCD, such that normal operation current densities will not trigger transport limitation and the lithium dendrite penetration. It is noteworthy that highly densified electrolyte pellets (relative density > 95%) are critical to prevent metal growth through percolated pores, especially in thinner electrolytes. Rational engineering of grain boundaries and promoting uniform flux distribution at the macroscopic Li/SSE interface are beneficial to avoid localized diffusion-limited metal penetrations.

Supporting Information

The Supporting Information is available free of charge online at ACS Energy Letters.

Experimental methods, analysis of initial Li|LLZO interface, interfacial evolutions schematic and cut sample, three-electrode tests, Nyquist plots with extracted resistance and capacitance values, extracted values and Nyquist plots during relaxation process with and without pressure, voltammograms for different thicknesses at different scan rates with and without concurrent EIS, chronopotentiometry curve during penetration, Randles-Sevcik Equation and limiting current calculations, areal capacity at current peaks, SEM of different relative densities with corresponding voltammograms and XRD of LLZO (pdf)

Data availability

The data that support the findings of this study are available from the corresponding author upon reasonable request.

Author contributions

P.B. designed and supervised the study and led the theoretical analysis. P.B., L.W., and R.G. synthesized the LLZTO powders and sintered the pellets. R.G. fabricated the cells, performed the electrochemical tests and microscopy characterization, and analyzed the data. J.G. contributed to the initial experiments. Y.L. performed the XRD characterization. P.B. and R.G. wrote and revised the manuscript.

Competing interests

The authors declare no competing financial interests.

Acknowledgment

This work is supported by two National Science Foundation Grants (Award No. 1934122 and 2203994). P.B. acknowledges the faculty startup support from Washington University in St. Louis. The materials characterization experiments were partially supported by IMSE (Institute of Materials Science and Engineering) at Washington University in St. Louis. The authors thank Dr. James Schilling and Dr. James Buckley for their help with the diamond saw.

References

- (1) Sharafi, A.; Haslam, C. G.; Kerns, R. D.; Wolfenstine, J.; Sakamoto, J. Controlling and Correlating the Effect of Grain Size with the Mechanical and Electrochemical Properties of Li7La3Zr2O12 Solid-State Electrolyte. *J. Mater. Chem. A* **2017**, *5* (40), 21491–21504. https://doi.org/10.1039/c7ta06790a.
- (2) Zhao, Q.; Stalin, S.; Zhao, C. Z.; Archer, L. A. Designing Solid-State Electrolytes for Safe, Energy-Dense Batteries. *Nat. Rev. Mater.* 2020, 5 (3), 229–252. https://doi.org/10.1038/s41578-019-0165-5.
- (3) Lu, Y.; Zhao, C. Z.; Yuan, H.; Cheng, X. B.; Huang, J. Q.; Zhang, Q. Critical Current Density in Solid-State Lithium Metal Batteries: Mechanism, Influences, and Strategies. *Adv. Funct. Mater.* **2021**, *2009925*, 1–33. https://doi.org/10.1002/adfm.202009925.
- (4) Shen, F.; Dixit, M. B.; Xiao, X.; Hatzell, K. B. Effect of Pore Connectivity on Li Dendrite Propagation within LLZO Electrolytes Observed with Synchrotron X-Ray Tomography.

 **ACS Energy Lett. 2018, 3 (4), 1056–1061. https://doi.org/10.1021/acsenergylett.8b00249.
- (5) Cheng, E. J.; Sharafi, A.; Sakamoto, J. Intergranular Li Metal Propagation through Polycrystalline Li6.25Al0.25La3Zr2O12 Ceramic Electrolyte. *Electrochim. Acta* 2017, 223, 85–91. https://doi.org/10.1016/j.electacta.2016.12.018.
- (6) Lu, Y.; Huang, X.; Ruan, Y.; Wang, Q.; Kun, R.; Yang, J.; Wen, Z. An: In Situ Element Permeation Constructed High Endurance Li-LLZO Interface at High Current Densities. *J. Mater. Chem. A* **2018**, *6* (39), 18853–18858. https://doi.org/10.1039/c8ta07241h.
- (7) Shen, F.; Dixit, M.; Xiao, X.; Hatzell, K. The Effect of Pore Connectivity on Li Dendrite

- Propagation Within LLZO Electrolytes Observed with Synchrotron X-Ray Tomography
 The Effect of Pore Connectivity on Li Dendrite Propagation Within LLZO X-Ray Science
 Division, Advanced Photon Source, Argonne. **2018**, 1–7.
- (8) Cheng, L.; Chen, W.; Kunz, M.; Persson, K.; Tamura, N.; Chen, G.; Doeff, M. Effect of Surface Microstructure on Electrochemical Performance of Garnet Solid Electrolytes. *ACS Appl. Mater. Interfaces* **2015**, *7* (3), 2073–2081. https://doi.org/10.1021/am508111r.
- (9) Pesci, F. M.; Brugge, R. H.; Hekselman, A. K. O.; Cavallaro, A.; Chater, R. J.; Aguadero, A. Elucidating the Role of Dopants in the Critical Current Density for Dendrite Formation in Garnet Electrolytes. *J. Mater. Chem. A* 2018, 6 (40), 19817–19827. https://doi.org/10.1039/c8ta08366e.
- (10) Zheng, C.; Ruan, Y.; Su, J.; Song, Z.; Xiu, T.; Jin, J.; Badding, M. E.; Wen, Z. Grain Boundary Modification in Garnet Electrolyte to Suppress Lithium Dendrite Growth. Chem. Eng. J. 2021, 411 (December 2020), 128508.
 https://doi.org/10.1016/j.cej.2021.128508.
- (11) Huang, X.; Lu, Y.; Guo, H.; Song, Z.; Xiu, T.; Badding, M. E.; Wen, Z. None-Mother-Powder Method to Prepare Dense Li-Garnet Solid Electrolytes with High Critical Current Density. ACS Appl. Energy Mater. 2018, 1 (10), 5355–5365.
 https://doi.org/10.1021/acsaem.8b00976.
- (12) Suzuki, Y.; Kami, K.; Watanabe, K.; Watanabe, A.; Saito, N.; Ohnishi, T.; Takada, K.; Sudo, R.; Imanishi, N. Transparent Cubic Garnet-Type Solid Electrolyte of Al2O3-Doped Li7La3Zr2O12. *Solid State Ionics* **2015**, *278*, 172–176. https://doi.org/10.1016/j.ssi.2015.06.009.

- (13) Krauskopf, T.; Hartmann, H.; Zeier, W. G.; Janek, J. Toward a Fundamental Understanding of the Lithium Metal Anode in Solid-State Batteries - An Electrochemo-Mechanical Study on the Garnet-Type Solid Electrolyte Li 6.25 Al 0.25 La 3 Zr 2 O 12. ACS Appl. Mater. Interfaces 2019, 11 (15), 14463–14477. https://doi.org/10.1021/acsami.9b02537.
- (14) Kazyak, E.; Garcia-Mendez, R.; LePage, W. S.; Sharafi, A.; Davis, A. L.; Sanchez, A. J.; Chen, K. H.; Haslam, C.; Sakamoto, J.; Dasgupta, N. P. Li Penetration in Ceramic Solid Electrolytes: Operando Microscopy Analysis of Morphology, Propagation, and Reversibility. *Matter* 2020, 2 (4), 1025–1048. https://doi.org/10.1016/j.matt.2020.02.008.
- (15) Liu, X.; Garcia-Mendez, R.; Lupini, A. R.; Cheng, Y.; Hood, Z. D.; Han, F.; Sharafi, A.; Idrobo, J. C.; Dudney, N. J.; Wang, C.; Ma, C.; Sakamoto, J.; Chi, M. Local Electronic Structure Variation Resulting in Li 'Filament' Formation within Solid Electrolytes. *Nat. Mater.* 2021. https://doi.org/10.1038/s41563-021-01019-x.
- (16) Han, F.; Westover, A. S.; Yue, J.; Fan, X.; Wang, F.; Chi, M.; Leonard, D. N.; Dudney, N. J.; Wang, H.; Wang, C. High Electronic Conductivity as the Origin of Lithium Dendrite Formation within Solid Electrolytes. *Nat. Energy* 2019, *4* (3), 187–196. https://doi.org/10.1038/s41560-018-0312-z.
- (17) Kasemchainan, J.; Zekoll, S.; Spencer Jolly, D.; Ning, Z.; Hartley, G. O.; Marrow, J.; Bruce, P. G. Critical Stripping Current Leads to Dendrite Formation on Plating in Lithium Anode Solid Electrolyte Cells. *Nat. Mater.* 2019, *18* (10), 1105–1111. https://doi.org/10.1038/s41563-019-0438-9.
- (18) Krauskopf, T.; Dippel, R.; Hartmann, H.; Peppler, K.; Mogwitz, B.; Richter, F. H.; Zeier,

- W. G.; Janek, J. Lithium-Metal Growth Kinetics on LLZO Garnet-Type Solid Electrolytes. *Joule* **2019**, *3* (8), 2030–2049. https://doi.org/10.1016/j.joule.2019.06.013.
- (19) Wang, M. J.; Choudhury, R.; Sakamoto, J. Characterizing the Li-Solid-Electrolyte
 Interface Dynamics as a Function of Stack Pressure and Current Density. *Joule* 2019, 3
 (9), 2165–2178. https://doi.org/10.1016/j.joule.2019.06.017.
- (20) Chen, C.; Wang, K.; He, H.; Hanc, E.; Kotobuki, M.; Lu, L. Processing and Properties of Garnet-Type Li7La3Zr2O12 Ceramic Electrolytes. *Small* **2022**. https://doi.org/10.1002/sml1.202205550.
- Zheng, H.; Wu, S.; Tian, R.; Xu, Z.; Zhu, H.; Duan, H.; Liu, H. Intrinsic Lithiophilicity of Li–Garnet Electrolytes Enabling High-Rate Lithium Cycling. *Adv. Funct. Mater.* 2020, 30 (6). https://doi.org/10.1002/adfm.201906189.
- (22) Bard, A.; Faulkner, L. Electrochemical Methods: Fundamentals and Applications; 2001; Vol. 2. https://doi.org/10.1016/B978-0-12-381373-2.00056-9.
- (23) Han, J. H.; Khoo, E.; Bai, P.; Bazant, M. Z. Over-Limiting Current and Control of Dendritic Growth by Surface Conduction in Nanopores. *Sci. Rep.* **2014**, *4*, 1–8. https://doi.org/10.1038/srep07056.
- (24) Kazyak, E.; William, S.; Haslam, C.; Sakamoto, J.; Dasgupta, N. P.; Kazyak, E.; Garciamendez, R.; Lepage, W. S.; Sharafi, A.; Davis, A. L.; Sanchez, A. J.; Chen, K.; Haslam, C.; Sakamoto, J.; Dasgupta, N. P. Li Penetration in Ceramic Solid Electrolytes: Operando Microscopy Analysis of Morphology, Propagation, and Reversibility Li Penetration in Ceramic Solid Electrolytes: Operando Microscopy Analysis of Morphology, Propagation, and Reversibility. *Matter* 2020, 2 (4), 1025–1048.

- https://doi.org/10.1016/j.matt.2020.02.008.
- (25) Krauskopf, T.; Mogwitz, B.; Hartmann, H.; Singh, D. K.; Zeier, W. G.; Janek, J. The Fast Charge Transfer Kinetics of the Lithium Metal Anode on the Garnet-Type Solid Electrolyte Li6.25Al0.25La3Zr2O12. *Adv. Energy Mater.* **2020**, *10* (27). https://doi.org/10.1002/aenm.202000945.
- (26) Zhang, X.; Wang, Q. J.; Harrison, K. L.; Roberts, S. A.; Harris, S. J. Pressure-Driven Interface Evolution in Solid-State Lithium Metal Batteries. *Cell Reports Phys. Sci.* 2020, 1 (2), 100012. https://doi.org/10.1016/j.xcrp.2019.100012.
- (27) Lee, K.; Kazyak, E.; Wang, M. J.; Dasgupta, N. P.; Sakamoto, J. Analyzing Void Formation and Rewetting of Thin in Situ -Formed Li Anodes on LLZO. *Matter* **2022**. https://doi.org/10.1016/j.joule.2022.09.009.
- (28) Taylor, N. J.; Stangeland-Molo, S.; Haslam, C. G.; Sharafi, A.; Thompson, T.; Wang, M.; Garcia-Mendez, R.; Sakamoto, J. Demonstration of High Current Densities and Extended Cycling in the Garnet Li7La3Zr2O12 Solid Electrolyte. *J. Power Sources* **2018**, *396* (April), 314–318. https://doi.org/10.1016/j.jpowsour.2018.06.055.
- (29) Wachter-Welzl, A.; Wagner, R.; Rettenwander, D.; Taibl, S.; Amthauer, G.; Fleig, J. Microelectrodes for Local Conductivity and Degradation Measurements on Al Stabilized Li7La3Zr2O12 Garnets. *J. Electroceramics* 2017, 38 (2–4), 176–181. https://doi.org/10.1007/s10832-016-0058-6.
- (30) Müller, M.; Schmieg, J.; Dierickx, S.; Joos, J.; Weber, A.; Gerthsen, D.; Ivers-Tiffée, E. Reducing Impedance at a Li-Metal Anode/Garnet-Type Electrolyte Interface
 Implementing Chemically Resolvable in Layers. ACS Appl. Mater. Interfaces 2022, 14

- (12), 14739–14752. https://doi.org/10.1021/acsami.1c25257.
- (31) David, I. N.; Thompson, T.; Wolfenstine, J.; Allen, J. L.; Sakamoto, J. Microstructure and Li-Ion Conductivity of Hot-Pressed Cubic Li7la3Zr2O12. *J. Am. Ceram. Soc.* 2015, 98
 (4), 1209–1214. https://doi.org/10.1111/jace.13455.
- (32) Thompson, T.; Sharafi, A.; Johannes, M. D.; Huq, A.; Allen, J. L.; Wolfenstine, J.; Sakamoto, J. A Tale of Two Sites: On Defining the Carrier Concentration in Garnet-Based Ionic Conductors for Advanced Li Batteries. *Adv. Energy Mater.* **2015**, *5* (11), 1–9. https://doi.org/10.1002/aenm.201500096.
- (33) Bai, P.; Li, J.; Brushett, F. R.; Bazant, M. Z. Transition of Lithium Growth Mechanisms in Liquid Electrolytes. *Energy Environ. Sci.* **2016**, *9* (10), 3221–3229. https://doi.org/10.1039/c6ee01674j.
- (34) Lee, Y.; Ma, B.; Bai, P. Concentration Polarization and Metal Dendrite Initiation in Isolated Electrolyte Microchannels. *Energy Environ. Sci.* 2020, 13 (10), 3504–3513. https://doi.org/10.1039/d0ee01874k.
- (35) Ma, B.; Bai, P. Fast Charging Limits of Ideally Stable Metal Anodes in Liquid Electrolytes. *Adv. Energy Mater.* **2022**, *12* (9), 1–9. https://doi.org/10.1002/aenm.202102967.
- (36) Squires, A. G.; Scanlon, D. O.; Morgan, B. J. Native Defects and Their Doping Response in the Lithium Solid Electrolyte Li7La3Zr2O12. *Chem. Mater.* 2020, 32 (5), 1876–1886. https://doi.org/10.1021/acs.chemmater.9b04319.
- (37) Monroe, C.; Newman, J. Dendrite Growth in Lithium/Polymer Systems. J. Electrochem.

- Soc. 2003, 150 (10), A1377. https://doi.org/10.1149/1.1606686.
- (38) Li, G.; Monroe, C. W. Dendrite Nucleation in Lithium-Conductive Ceramics. *Phys. Chem. Chem. Phys.* **2019**, *21* (36), 20354–20359. https://doi.org/10.1039/c9cp03884a.
- (39) Rosso, M.; Brissot, C.; Teyssot, A.; Dollé, M.; Sannier, L.; Tarascon, J. M.; Bouchet, R.; Lascaud, S. Dendrite Short-Circuit and Fuse Effect on Li/Polymer/Li Cells. *Electrochim*. *Acta* **2006**, *51* (25), 5334–5340. https://doi.org/10.1016/j.electacta.2006.02.004.
- (40) Newman, J.; Thomas-alyea, K. E. Electrochemical Systems. wiley 2004, No. 3rd.
- (41) Kubicek, M.; Wachter-Welzl, A.; Rettenwander, D.; Wagner, R.; Berendts, S.; Uecker, R.; Amthauer, G.; Hutter, H.; Fleig, J. Oxygen Vacancies in Fast Lithium-Ion Conducting Garnets. *Chem. Mater.* 2017, 29 (17), 7189–7196.
 https://doi.org/10.1021/acs.chemmater.7b01281.
- (42) Murch, G. E. The Haven Ratio in Fast Ionic Conductors. *Solid State Ionics* **1982**, *7* (3), 177–198.
- (43) He, X.; Zhu, Y.; Mo, Y. Origin of Fast Ion Diffusion in Super-Ionic Conductors. *Nat. Commun.* **2017**, *8* (May), 1–7. https://doi.org/10.1038/ncomms15893.
- (44) Di Stefano, D.; Miglio, A.; Robeyns, K.; Filinchuk, Y.; Lechartier, M.; Senyshyn, A.;
 Ishida, H.; Spannenberger, S.; Prutsch, D.; Lunghammer, S.; Rettenwander, D.;
 Wilkening, M.; Roling, B.; Kato, Y.; Hautier, G. Superionic Diffusion through Frustrated
 Energy Landscape. *Chem* 2019, 5 (9), 2450–2460.
 https://doi.org/10.1016/j.chempr.2019.07.001.
- (45) Hitz, G. T.; McOwen, D. W.; Zhang, L.; Ma, Z.; Fu, Z.; Wen, Y.; Gong, Y.; Dai, J.;

- Hamann, T. R.; Hu, L.; Wachsman, E. D. High-Rate Lithium Cycling in a Scalable Trilayer Li-Garnet-Electrolyte Architecture. *Mater. Today* **2019**, *22* (February), 50–57. https://doi.org/10.1016/j.mattod.2018.04.004.
- (46) De Klerk, N. J. J.; Wagemaker, M. Space-Charge Layers in All-Solid-State Batteries; Important or Negligible? *ACS Appl. Energy Mater.* **2018**, *1* (10), 5609–5618. https://doi.org/10.1021/acsaem.8b01141.
- (47) Yamamoto, K.; Iriyama, Y.; Asaka, T.; Hirayama, T.; Fujita, H.; Fisher, C. A. J.; Nonaka, K.; Sugita, Y.; Ogumi, Z. Dynamic Visualization of the Electric Potential in an All-Solid-State Rechargeable Lithium Battery. *Angew. Chemie Int. Ed.* 2010, 49 (26), 4414–4417. https://doi.org/10.1002/anie.200907319.
- (48) Yamamoto, K.; Iriyama, Y.; Hirayama, T. Operando Observations of Solid-State Electrochemical Reactions in Li-Ion Batteries by Spatially Resolved TEM EELS and Electron Holography. *Microscopy* **2017**, *66* (1), 50–61. https://doi.org/10.1093/jmicro/dfw043.
- (49) Nomura, Y.; Yamamoto, K.; Hirayama, T.; Ouchi, S.; Igaki, E.; Saitoh, K. Direct Observation of a Li-Ionic Space-Charge Layer Formed at an Electrode/Solid-Electrolyte Interface. *Angew. Chemie - Int. Ed.* 2019, 58 (16), 5292–5296. https://doi.org/10.1002/anie.201814669.
- (50) Lampert, M. A.; Schilling, R. B. Current Injection in Solids: The Regional Approximation Method. *Semicond. Semimetals* **1970**, *6* (C), 1–351. https://doi.org/10.1016/S0080-8784(08)62630-7.
- (51) Chazalviel, J. N. Electrochemical Aspects of the Generation of Ramified Metallic

- Electrodeposits. *Phys. Rev. A* **1990**, *42* (12), 7355–7367. https://doi.org/10.1103/PhysRevA.42.7355.
- (52) Rubinstein, S. M.; Manukyan, G.; Staicu, A.; Rubinstein, I.; Zaltzman, B.; Lammertink, R. G. H.; Mugele, F.; Wessling, M. Direct Observation of a Nonequilibrium Electro-Osmotic Instability. *Phys. Rev. Lett.* 2008, 101 (23), 1–4. https://doi.org/10.1103/PhysRevLett.101.236101.
- (53) Huth, J. M.; Swinney, H. L.; McCormick, W. D.; Kuhn, A.; Argoul, F. Role of Convection in Thin-Layer Electrodeposition. *Phys. Rev. E* 1995, 51 (4), 3444–3458. https://doi.org/10.1103/PhysRevE.51.3444.
- (54) Neusel, C.; Jelitto, H.; Schmidt, D.; Janssen, R.; Felten, F.; Schneider, G. A. Dielectric Breakdown of Alumina Single Crystals. *J. Eur. Ceram. Soc.* **2012**, *32* (5), 1053–1057. https://doi.org/10.1016/j.jeurceramsoc.2011.11.013.
- (55) Porz, L.; Swamy, T.; Sheldon, B. W.; Rettenwander, D.; Frömling, T.; Thaman, H. L.; Berendts, S.; Uecker, R.; Carter, W. C.; Chiang, Y. M. Mechanism of Lithium Metal Penetration through Inorganic Solid Electrolytes. *Adv. Energy Mater.* **2017**, *7* (20). https://doi.org/10.1002/aenm.201701003.
- (56) Hatzell, K. B.; Chen, X. C.; Cobb, C. L.; Dasgupta, N. P.; Dixit, M. B.; Marbella, L. E.;
 McDowell, M. T.; Mukherjee, P. P.; Verma, A.; Viswanathan, V.; Westover, A. S.; Zeier,
 W. G. Challenges in Lithium Metal Anodes for Solid-State Batteries. *ACS Energy Lett.*2020, 5 (3), 922–934. https://doi.org/10.1021/acsenergylett.9b02668.